ORIGINAL PAPER

Improvement of the accuracy of active seismic tomography by eliminating blasting delay in coal mines

Siyuan Gong[1] · Jing Li[2] · Kefeng Shangguan[3] · Zaijun Xue[3]

Abstract

Active seismic velocity tomography as a powerful tool in inferring stress states has been widely used in the assessment of dynamic hazards such as rockbursts. However, the pre-set blasting delay in the detonators used in active tomography practice renders the tomographic results inaccurate. In this study, the influence of blasting delay on active inversions was analysed quantitatively using an inversion model. Thereafter, a method was proposed to eliminate the delay. Delay-eliminated seismic data was applied to an active tomography operation in panel LW3310 of a coal mine in Shandong province, China. Inversion results show that there were four high-velocity areas in the panel. These areas were certified as being high-stress areas through field observations, which proves the reliability of the active velocity tomography technique and the accuracy of the proposed delay elimination method.

Keywords Coal mining · Rockburst · Active seismic tomography · Blasting delay elimination

Introduction

Seismic velocity tomography is a powerful tool for inferring rock stress characteristics by reconstructing the wave velocity distribution (Begg et al. 2009; Cao et al. 2015; Friedel et al. 1995; Sheehan et al. 2014; Ustaszewski et al. 2012; Young and Maxwell 1992). This technique has been used in determining high-stress areas and predicting rockburst hazards in mining (Gong et al. 2019; Hosseini et al. 2011, 2012; Li et al. 2017; Wang et al. 2018). According to the types of wave sources, seismic tomography can be classified as "active" and "passive" (Lurka 2008; Luxbacher et al. 2008). Passive tomography uses mining-induced microseismic events as its sources, while the sources for

✉ Jing Li
Jing.li2@monash.edu

1   Laboratory of Mine Earthquake Monitoring and Prevention, School of Mines, China University of Mining and Technology, Xuzhou 221116, Jiangsu, China

2   Department of Civil Engineering, Monash University, Melbourne, VIC 3800, Australia

3   Huating Coal Industry Group Co., Ltd., Pingliang 744000, Gansu, China
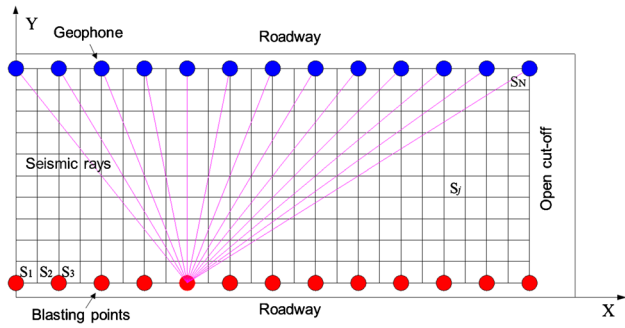
active tomography are normally produced by explosives at known positions (Cao et al. 2015; Su et al. 2020). One of the prominent advantages of active tomography is that it can provide important assessments before coal mining by analysing controllable human-made vibration signals (He et al. 2011). Due to its precise source locations, identified study areas, and rapid and accurate inversion results, active velocity tomography has been paid increasing research attention.

For an active tomography test in a coal mine, explosives are generally arranged along the roadway as seismic signals, and geophones are arranged along the other roadway as receivers. Geophones can record vibration signals generated by the explosion in the coal-rock mass. The velocity distribution in the coal and rock mass can be inversed according to the first arrival time of different wave sources. The layout of blasting points and geophones in an underground coal mining is shown in Fig. 1.

The travel time T from blasting points S to geophones R represents a line integral of wave slowness P (inverse of velocity v), which can be expressed by $T_i = \int_{L_i} \frac{ds}{V(x,y)} = \int_{L_i} S(x,y)ds$ (Hosseini et al. 2012; Lurka 2008), where L_i is the i th ray path from source to geophones. To solve the equation, the inversion region can be divided into M grids, and travel time T_i in the i th grid can be described as $T_i = \sum_{j=1}^{M} d_{ij}S_j (i = 1, 2 \dots N)$, where d_{ij} is the distance

Fig. 1 Principle of active seismic velocity tomographic practice in underground coal mining

travelled by the i th ray through grid j, and N is the total number of rays. Apparently, accurately determining the travel time plays a crucial role in inversion calculation. However, mine explosives normally have a pre-set blasting delay due to the presence of delay composition, which means that travel time data recorded by geophones are not the actual propagation time of P-waves. Moreover, different types of explosives with different delays are likely to be used in one active tomographic operation, which maybe reduces the accuracy of inversion results.

This study investigates the effect of blasting delay in detail using an inversion model. Then, a least squares regression method is adopted to eliminate blasting delay based on the relationship between P-wave travel time and its propagation distance. The delay-eliminated seismic data is also applied in an active tomography test in a coal mine.

Methodology

Inversion model

An inversion model is established to investigate the effect of blasting delay on active tomography, as shown in Fig. 2a. 6×5 grids (N1, N2, …, N30) are created in the model, and each grid measures 20 m × 20 m in the X- and Y-directions, respectively. The coordinates of blasting points (B1, B2, B3 and B4) and receivers (R1, R2, R3 and R4) are listed in Table 1. Thirty random initial velocities ranging from 3.40 to 5.40 are distributed within this area, and the velocity contour is obtained by using the Kriging interpolation method (Fig. 2b). Two high-velocity regions are observed in the inversion model, namely N8 and N22. Table 2 shows the travel time of each seismic ray, which can be calculated based on the wave velocity and the distance travelled by a ray passing through the mesh. It is noted that the travel time in Table 2 is the actual propagation time (without blasting delay) of P-waves from blasting points to geophones in the inversion model.

Table 1 Layout of blasting points and receivers in active inversion model

Blasting/geophone no	X-coordinate/m	Y-coordinate/m
B1	0	0
B2	40	0
B3	80	0
B4	120	0
R1	0	100
R2	40	100
R3	80	100
R4	120	100

Fig. 2 Established active tomography model (**a**) (grid numbers represented by N1, N2, …, N30, velocity values represented by numerical values in every grid, unit: km/s) and velocity cloud image in active inversion model (**b**)
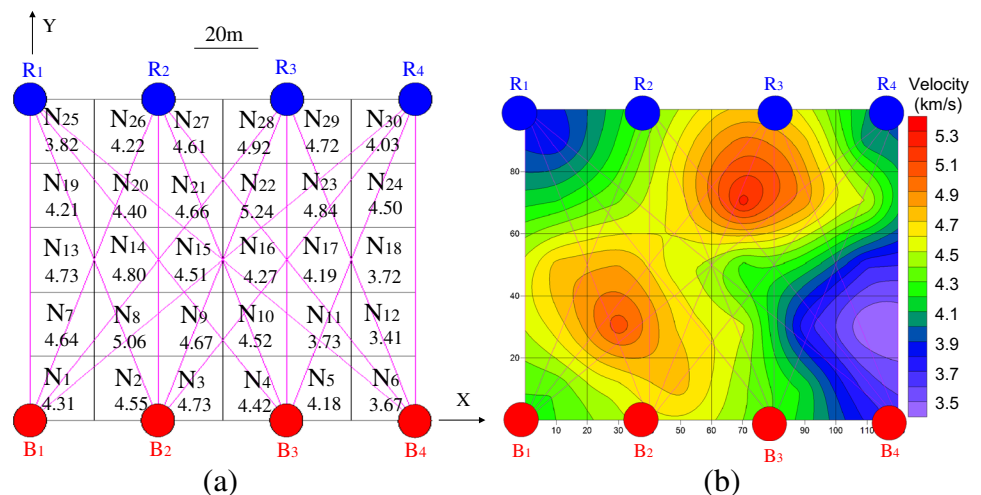
Table 2 Travel time of P-waves after blasting in active tomography model (unit: ms)

Travel time/ms	B_1	B_2	B_3
R1	23.1652	24.2676	29.4237
R2	24.1611	21.5758	23.8446
R3	27.1763	22.5661	23.2894
R4	34.5602	28.8386	26.5259

As mentioned above, the explosives used in coal mines usually have a blasting delay. Besides, two or more different types of detonators may be used in an active inversion operation. It may affect the inversion results due to the wrong P-wave travel time being applied in the tomographic algorithms. Therefore, the following two tests were conducted to study the effect of blasting delay on the inversion:

Test 1:   Adding different delay lengths from 1 to 6 ms to the actual P-wave travel time demonstrated in Table 2, and then reconstructing the velocity distribution.

Test 2:   Adding different delay combinations to the actual P-wave travel time demonstrated in Table 2, and then reconstructing the velocity distribution. The following six delay combinations were considered: (I) 1 ms of delay for B1 and B2, 5 ms of delay for B3 and B4; (II) 1 ms of delay for B1 and B3, 5 ms of delay for B2 and B4; (III) 1 ms of delay for B1 and B4, 5 ms of delay for B2 and B3; (IV) 1 ms of delay for B2 and B3, 5 ms of delay for B1 and B4; (V) 1 ms of delay for B2 and B4, 5 ms of delay for B1 and B3; and (VI) 1 ms of delay for B3 and B4, 5 ms of delay for B1 and B2.

Delay-eliminated method

For an active tomographic operation in a coal mine, the general relationship between recorded P-wave travel time and its propagation distance is shown in Fig. 3. There is a positive correlation between them, and all data are scattered near the red oblique line in the graph, but the line does not pass through the origin due to the existence of blasting delay. Without delay, the fit line should pass through the origin, as shown by the green line in Fig. 3. Therefore, the intercept of the fit line of the observed data is the delay. In view of this, the below method is used to calculate the delay.

Assuming vibration signals from a blasting point are recorded by n geophones in an active inversion test. The P-wave travel time recorded by the i th geophone is denoted by t_{p_i} ($i = 1, 2, …, n$). The distance between the blasting point and the geophones is described as r_i. The relationship among P-wave velocity v, P-wave travel time t_{p_i} and the delay t_d can be described as below:
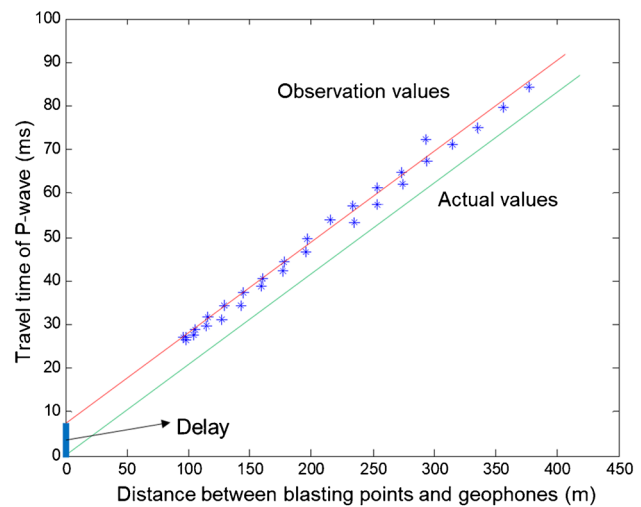

Fig. 3 Relationship between P-wave travel time and propagation time

$$\begin{cases} t_{p_1} = t_d + \frac{r_1}{v} \\ t_{p_2} = t_d + \frac{r_2}{v} \\ \dots\dots.. \\ t_{p_n} = t_d + \frac{r_n}{v} \end{cases} \rightarrow \begin{bmatrix} t_{p_1} \\ t_{p_2} \\ \dots \\ t_{p_n} \end{bmatrix} = \begin{bmatrix} 1 & r_1 \\ 1 & r_2 \\ \dots & \dots \\ 1 & r_n \end{bmatrix} \begin{bmatrix} t_d \\ \frac{1}{v} \end{bmatrix} \quad (1)$$

The v and t_d are obtained by the least-square linear fitting method (Reza and Sengupta 2017; Xu et al. 2018):

$$\frac{1}{v} = \frac{\sum_{i=1}^{n} r_i t_{p_i} - \frac{1}{n} \sum_{i=1}^{n} r_i \sum_{i=1}^{n} t_{p_i}}{\sum_{i=1}^{n} r_i^2 - \frac{1}{n}(\sum_{i=1}^{n} r_i^2)} \quad (2)$$

$$t_d = \frac{1}{n} \sum_{i=1}^{n} t_{p_i} - \frac{1}{v}\frac{1}{n} \sum_{i=1}^{n} r_i \quad (3)$$

The actual P-wave travel time t'_{pi} can be obtained by subtracting the detonator delay t_d from the recorded P-wave travel time t_{p_i}:

$$\begin{cases} t'_{p_1} = t_{p_1} - t_d \\ t'_{p_2} = t_{p_2} - t_d \\ \dots\dots \\ t'_{p_n} = t_{p_n} - t_d \end{cases} \quad (4)$$

According to the above steps, the delay for each blasting point can be obtained in turn, and then the actual P-wave travel time can also be obtained.

Applications

The selected coal panel (LW3310 in Xingcun Coal Mine) is situated in the south of Shandong province, China. The mining depth ranges from 1080 to 1125 m. The inclined length and strike length of the panel LW3310 are 680 m and 100 m, respectively (Fig. 4a). The north side of the panel borders LW5303 goaf. Some faults in the side of the track roadway were detected during roadway excavation, among which fault JF10-3 has a large down-throw of 5 m. To detect the stress distribution characteristics around WL3310, active velocity tomography was conducted from 12 to 14 May 2016. In the test, 31 blasting points (B1 to B31) with an explosive charge weighing 300 g each were arranged on the side of the track roadway. The blasting sequence is from B31 to B1 (Fig. 4b). Thirty-two geophones (S1 to S32) with a sampling rate of 4 kHz were arranged on the side of the transport roadway to receive blasting waves. Among these geophones, S1 is a standard one used to stamp the start time; thus, the P-wave travel time recorded by other geophones can be calculated by $T_i - T_1(i = 2, \ldots, 32)$. It should be noted that effective signals were recorded from other blasting points apart from the fact that blasting point B7 failed to detonate and geophone S24 did not record a signal.

The relationship between recorded P-wave travel time and propagation distance is shown in Fig. 5a. Two types of explosives with different delays were used in this active velocity tomographic practice marked explosive A and explosive B. The method proposed in the "Applications" section was used to eliminate the delay of detonators for the recorded waveform data. The blasting delay and wave velocity at all blasting points are calculated according to Eqs. (2) to (3), and the results are listed in Table 3. Blasting points B1 to B16 have short delays with values ranging from 0 to 10 ms. However, the delay at blasting points B17 to B30 is around 100 ms. The actual P-wave travel time can be obtained based on Eq. (4), and its relationship with propagation distance is shown in Fig. 5b. After the delay elimination, the velocity grouping phenomenon is not observed.

In the active tomography calculation, 34×8 grids were created in the inversion model, and each grid measured $20 \text{ m} \times 12 \text{ m}$ in the X- and Y-directions, respectively. To improve the accuracy of seismic tomography, high signal-to-noise ratio waveforms were selected for the tomographic algorithm, and finally, 775 seismic rays between geophones and blasting points were created. A simultaneous iterative reconstruction technique was chosen as an inversion algorithm in this study considering its good convergence.

Results and discussion

Figure 6 shows the influence of different delay lengths (test 1 in the "Inversion model" section) on inversion results. After adding a delay of 1 ms, 3 ms and 5 ms, the calculated wave velocity ranges are 3.44 to 4.77 km/s, 3.32 to 4.53 km/s and 3.04 to 4.32 km/s, respectively. Figure 7a shows that the delay reduces the overall velocity in the inversion region, and the longer the delay, the greater the decrease. However,
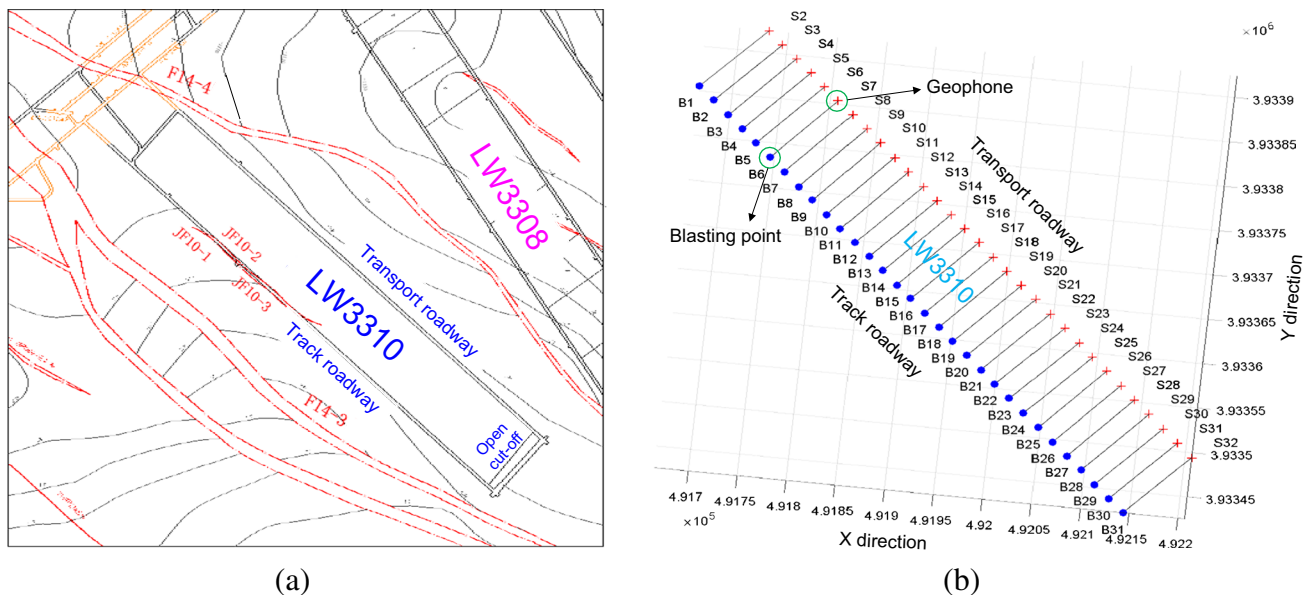

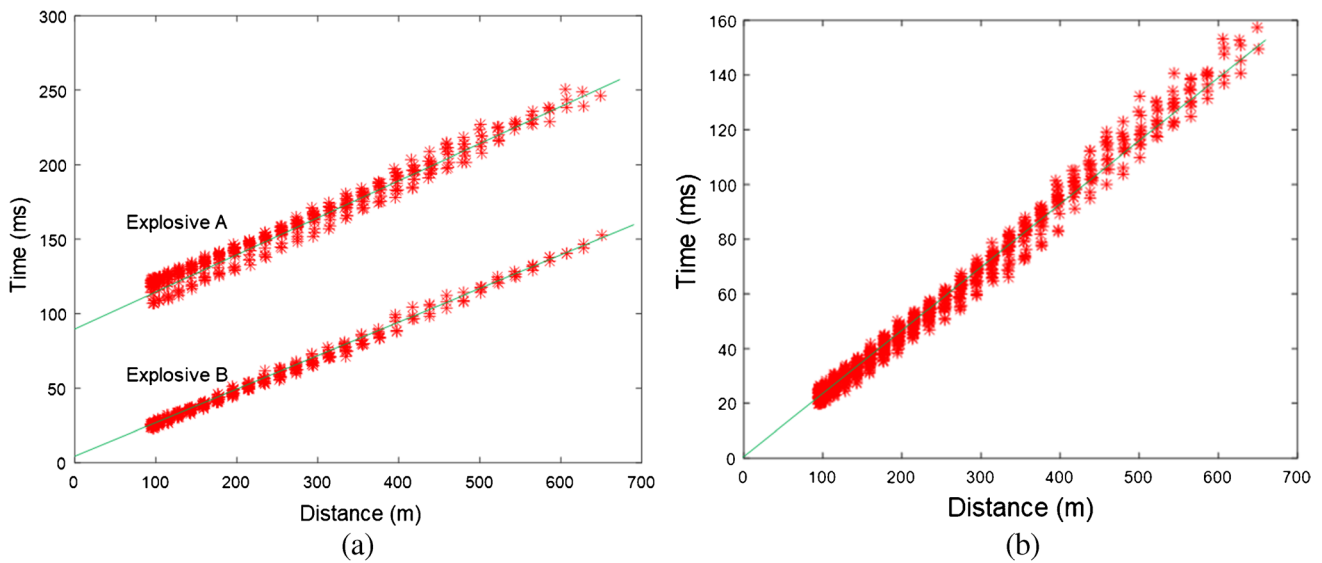**Fig. 4** Layout of the LW3310 working face (**a**) and layout of blasting points and receiver points (**b**)

Fig. 5 Relationship between P-wave travel time and distance before (**a**) and after (**b**) detonator delay elimination

Table 3 Calculated detonator delays and velocities

Blasting points	Delay/ms	Velocity/(km/s)	Blasting points	Delay/ms	Velocity/(km/s)
B1	3.4511	4.3860	B17	102.7377	4.6232
B2	0.9932	4.3046	B18	98.4446	4.4315
B3	4.5703	4.6344	B19	95.7212	4.0703
B4	3.8400	4.5018	B20	98.3144	4.1700
B5	2.5963	4.4197	B21	83.0102	4.1479
B6	4.3616	4.6519	B22	94.9545	4.1585
B8	2.2559	4.2718	B23	82.8277	4.0333
B9	1.4517	4.0357	B24	96.8706	4.0841
B10	3.2937	4.3243	B25	95.0110	4.0103
B11	2.9292	4.3989	B26	93.8853	4.1033
B12	5.2199	4.7450	B27	93.8173	4.2935
B13	5.4574	4.8143	B28	98.2491	4.2256
B14	6.5663	4.8012	B29	97.1379	4.1594
B15	3.7796	4.5056	B30	96.1255	4.2155
B16	2.9435	4.4879	B31	88.4335	4.1507

the high-velocity regions undergo little significant change. Figure 7b shows the root-mean-square (RMS) error statistics of velocity value under different delays. There is a linear increasing relationship between the delay length and the inversion error. In other words, the longer the delay, the greater the inversion error. According to the above analysis, we can get the enlightenment: without eliminating the blasting delay, the velocity distribution of coal-rock mass obtained by active tomographic detection may be lower than that in reality, for example, some low/medium-wave velocity areas may be potential high-wave velocity areas.

Figure 8 shows the influence of different delay combinations (test 2 in the "Inversion model" section) on inversion results. After adding delay combinations I, III and V, the calculated wave velocity ranges are 3.00+ to 6.36 km/s, 2.95 to 7.35 km/s and 2.87 to 7.05 km/s, respectively. Under different delay combinations, the range of wave velocity changes significantly, and the location of high-wave velocity regions also change in an unpredictable manner. In addition, compared with the model velocity (without delay), the wave velocity in grids N7 to N30 is generally low, but the trend is similar. However, the velocity changes in grids N1 to N6 are anomalous: some of the wave velocities are much higher than the model velocity, while some are much lower (see Fig. 9a). Figure 9b shows the RMS error of wave velocity under different delay combinations. The inversion
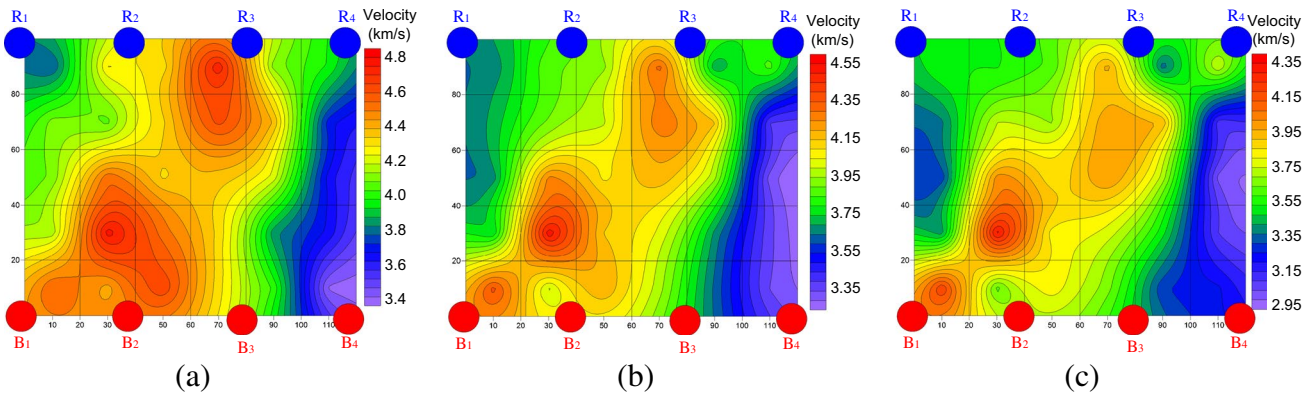
Fig. 6 Inversion results after adding a delay of 1 ms (**a**), 3 ms (**b**) and 5 ms (**c**)

Fig. 7 Comparison of inversion results (**a**) and inversion errors (**b**) with different delays
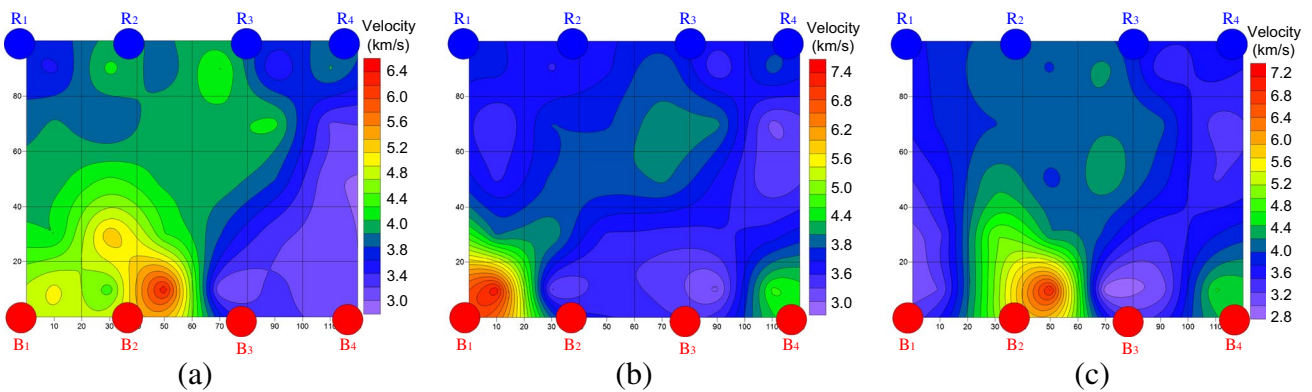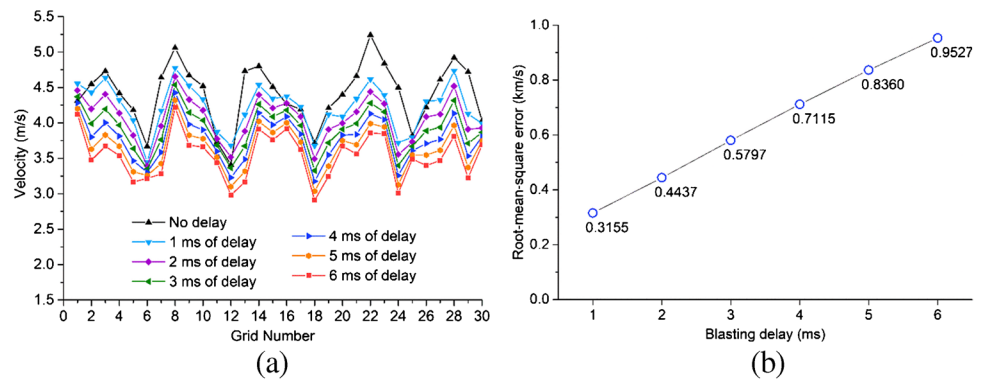

Fig. 8 Inversion results after adding delay combination I (**a**), combination III (**b**) and combination V (**c**)

error range under different delay combinations is 0.6149 to 0.9992 km/s, indicating that the error fluctuation is large. The above analysis indicates that different delay combinations exert a significant influence on the tomographic results, not only significantly increasing the inversion error, but also causing unpredictable velocity changes. In other words, the high-wave velocity area obtained by inversion under different delay combinations may be a potential low-wave velocity area, while the low-wave velocity area may also be a potential high-wave velocity area. Therefore, in the actual active tomography operations in a coal mine, the obtained velocity distribution may be unreliable if the effect of delay combinations is ignored.

Figure 10a shows the tomographic results before blasting delay was eliminated. Different colours represent the magnitude of wave velocities. According to Fig. 10a, high-wave velocity regions are mainly located near faults. The distribution of high- and low-wave velocity regions is obvious,

Fig. 9 Comparison of inversion results (**a**) and inversion errors (**b**) with different delay combinations
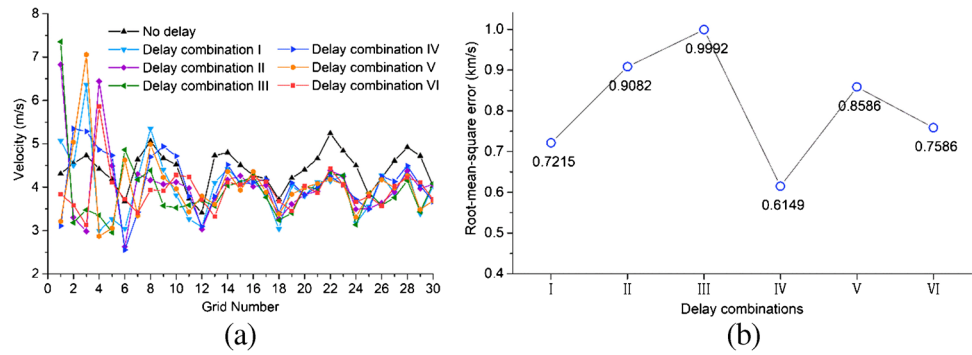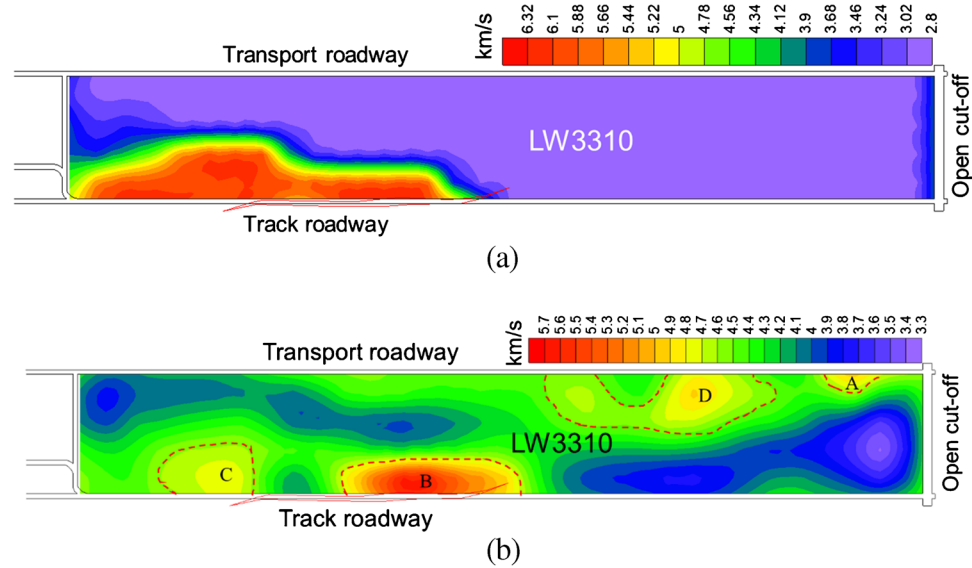

(a)

(b)

Fig. 10 Inversion result before (**a**) and after (**b**) eliminating delay

(a)

(b)

and gradient of wave velocity is large ranging from 2.8 to 6.32 km/s. Unpredictable velocity anomalies appear in the inversion region due to different delay combinations, which fails to reflect the true stress state in a coal-rock mass.

Actual P-wave travel time data were also used for active tomographic calculation after delay elimination, and the result is demonstrated in Fig. 10b. There are four high-stress areas detected in panel LW3310 (i.e. areas A, B, C and D). Among them, area B has the highest wave velocity which corresponds to the highest stress concentration. The fault JF10-3 within area B was activated by roadway driving, resulting in regional stress concentration (Sainoki et al. 2017; Sidorenko et al. 2019; Wu et al. 2017). In addition, coal seam thinning had occurred in this area according to the field investigation. Stresses tend to increase in coal seam thinning areas (Yang et al. 2018; Zhu et al. 2016). Therefore, the wave velocity anomaly in area B is mainly affected by fault activation and coal thickness variation. High-velocity area C lies in the syncline axis. The horizontal stress exhibits significantly increasing trend for coal mass in the syncline axis (Guo et al. 2017; Shepherd et al. 1981; Wang et al. 2016). Therefore, the syncline structure is the main reason

for the increase of the wave velocity in this area. For the high velocity areas A and D along the transport roadway of LW3310, high-stress areas are formed by transferred stress due to the excavation of nearby panel LW3308. The high-stress distribution in areas A and D is also consistent with the fact that the nut and anchor bolt on the side close to the transport roadway are tightly engaged and cannot be disassembled. According to the above analysis, the reliability of the inversion result of active velocity tomography after eliminating the delay is proved, and the accuracy of the delay elimination method at each detonator is also explained.

Conclusions

The pre-set blasting delay in the detonators renders the active velocity tomographic results inaccurate. In this study, an active tomography model was established to investigate the effect of blasting delay in two delay schemes. Experimental results show that, if all detonators have the same delay, the delay will reduce the overall velocity in the inversion region, and the longer this delay is, the greater the decrease in wave

velocity. If detonators have different pre-set delays, different delay combinations significantly increase the inversion error. According to the relationship between P-wave travel time and propagation distance, a delay-elimination method was proposed by least squares linear fitting. The proposed method was successfully used to eliminate delay in seismic data in an active tomography operation in panel LW3310 of Xingcun Coal Mine, Shandong province, China. After that, delay-eliminated seismic data were also applied to tomographic calculation. Inversion results successfully reveal high-stress areas in the studied panel.

Data Availability The authors confirm that the data supporting the findings of this study are available within the article.

Declarations

Conflict of interest The authors declare that they have no competing interests.

References

Begg GC, Griffin WL, Natapov LM, O'Reilly SY, Grand SP, O'Neill CJ, Hronsky JMA, Djomani YP, Swain CJ, Deen T, Bowden P (2009) The lithospheric architecture of Africa: seismic tomography, mantle petrology, and tectonic evolution. Geosphere 5:23–50

Cao A, Dou L, Cai W, Gong S, Liu S, Jing G (2015) Case study of seismic hazard assessment in underground coal mining using passive tomography. Int J Rock Mech Min Sci 78:1–9

Friedel MJ, Jackson MJ, Scott DF, Williams TJ, Olson MS (1995) 3-D tomographic imaging of anomalous conditions in a deep silver mine. J Appl Geophys 34:1–21

Gong S-Y, Li J, Ju F, Dou L-M, He J, Tian X-Y (2019) Passive seismic tomography for rockburst risk identification based on adaptive-grid method. Tunn Undergr Space Technol 86:198–208

Guo W-Y, Zhao T-B, Tan Y-L, Yu F-H, Hu S-C, Yang F-Q (2017) Progressive mitigation method of rock bursts under complicated geological conditions. Int J Rock Mech Min Sci 96:11–22

He H, Dou L, Li X, Qiao Q, Chen T, Gong S (2011) Active velocity tomography for assessing rock burst hazards in a kilometer deep mine. Min Sci Technol (china) 21:673–676

Hosseini N, Oraee K, Shahriar K, Goshtasbi K (2011) Studying the stress redistribution around the longwall mining panel using passive seismic velocity tomography and geostatistical estimation. Arab J Geosci 6:1407–1416

Hosseini N, Oraee K, Shahriar K, Goshtasbi K (2012) Passive seismic velocity tomography and geostatistical simulation on longwall mining panel/Tomografia pasywna pola prędkości i symulacje geostatystyczne w obrębie pola ścianowego. Arch Min Sci 57:139–155

Li J, Gong S-Y, He J, Cai W, Zhu G-A, Wang C-B, Chen T (2017) Spatio-temporal assessments of rockburst hazard combining b values and seismic tomography. Acta Geophys 65:77–88

Lurka A (2008) Location of high seismic activity zones and seismic hazard assessment in Zabrze Bielszowice coal mine using passive tomography. J China Univ Min Technol 18:177–181

Luxbacher K, Westman E, Swanson P, Karfakis M (2008) Three-dimensional time-lapse velocity tomography of an underground longwall panel. Int J Rock Mech Min Sci 45:478–485

Reza A, Sengupta AS (2017) Least square ellipsoid fitting using iterative orthogonal transformations. Appl Math Comput 314:349–359

Sainoki A, Mitri HS, Chinnasane D (2017) Characterization of aseismic fault-slip in a deep hard rock mine through numerical modelling: case study. Rock Mech Rock Eng 50:2709–2729

Sheehan AF, de la Torre TL, Monsalve G, Abers GA, Hacker BR (2014) Physical state of Himalayan crust and uppermost mantle: constraints from seismic attenuation and velocity tomography. J Geophys Res: Solid Earth 119:567–580

Shepherd J, Rixon LK, Griffiths L (1981) Outbursts and geological structures in coal mines: a review. Int J Rock Mech Min Sci Geomech Abstr 18(4):267–283

Sidorenko AA, Ivanov VV, Sidorenko SA (2019) Numerical simulation of rock massif stress state at normal fault at underground longwall coal mining. Int J Civ Eng Technol (IJCIET) 1:844–851

Su M, Liu Y, Xue Y, Qu C, Wang P, Zhao Y (2020) Detection method of pile foundation on subway lines based on cross-hole resistivity computed tomography. J Perform Constr Facilities 34(6):04020103

Ustaszewski K, Wu Y-M, Suppe J, Huang H-H, Chang C-H, Carena S (2012) Crust–mantle boundaries in the Taiwan-Luzon arc-continent collision system determined from local earthquake tomography and 1D models: implications for the mode of subduction polarity reversal. Tectonophysics 578:31–49

Wang G-F, Gong S-Y, Li Z-L, Dou L-M, Cai W, Mao Y (2016) Evolution of stress concentration and energy release before rock bursts: two case studies from Xingan coal mine, Hegang, China. Rock Mech Rock Eng 49:3393–3401

Wang G, Gong S, Dou L, Wang H, Cai W, Cao A (2018) Rockburst characteristics in syncline regions and microseismic precursors based on energy density clouds. Tunn Undergr Space Technol 81:83–93

Wu Q-S, Jiang L-S, Wu Q-L (2017) Study on the law of mining stress evolution and fault activation under the influence of normal fault. Acta Geodyn Geomater 14:357–369

Xu W, Chen W, Liang Y (2018) Feasibility study on the least square method for fitting non-Gaussian noise data. Physica A 492:1917–1930

Yang W, Wang H, Lin B, Wang Y, Mao X, Zhang J, Lyu Y, Wang M (2018) Outburst mechanism of tunnelling through coal seams and the safety strategy by using "strong-weak" coupling circle-layers. Tunn Undergr Space Technol 74:107–118

Young RP, Maxwell SC (1992) Seismic characterization of a highly stressed rock mass using tomographic imaging and induced seismicity. J Geophys Res 97(B9):12361-12373

Zhu G-A, Dou L-M, Li Z-L, Cai W, Kong Y, Li J (2016) Mining-induced stress changes and rock burst control in a variable-thickness coal seam. Arab J Geosci 9:365